Originally published as:

Geochemistry
Geophysics
Geosystems

G³

# Revising the spectral method as applied to modeling mantle dynamics

**A. G. Petrunin and M. K. Kaban**

*Helmholtz Centre Potsdam, GFZ German Research Centre for Geosciences, Telegrafenberg DE-14473, Potsdam, Germany (alexei@gfz-potsdam.de)*

*Schmidt Institute of Physics of the Earth, Moscow, Russia*

**I. Rogozhina**

*Helmholtz Centre Potsdam, GFZ German Research Centre for Geosciences, Telegrafenberg DE-14473, Potsdam, Germany*

**V. Trubitsyn**

*Schmidt Institute of Physics of the Earth, Moscow, Russia*

[1] The observed geoid, dynamic topography, and surface plate velocities are controlled by various factors such as density and viscosity variations in the Earth's mantle and strength of the lithosphere. Previous studies have shown that the geoid signal cannot be resolved in details within the framework of a simplified model of the mantle flow considering only radial viscosity variations. Thus, a modeling technique handling both radial and lateral variations of viscosity and other parameters should be used. The spectral method provides a high-accuracy semianalytical solution of the Navier-Stokes and Poisson equations when viscosity is only depth (radially) dependent. In this study, we present the numerical approach, built up on the substantially revised method originally proposed by Zhang and Christensen (1993), for solving the Navier-Stokes equation in the spectral domain with lateral variations of viscosity (LVV). This approach incorporates a number of numerical algorithms providing efficient calculations of the instantaneous Stokes flow in the sphere and taking into account the effects of LVV, self gravitation, and compressibility. In contrast to the traditionally used propagator method, our approach suggests a continuous integration over depth without introducing internal interfaces. Various numerical tests have been employed to test accuracy and efficiency of the proposed technique. Benchmarking of the code shows its ability to solve the mantle convection problems implying strong LVV with high resolution.

# 1. Introduction

[2] The spectral method is widely used for modeling of the instantaneous mantle flow, geoid, and stress field in the mantle since the pioneering work of *Hager and O'Connell* [1981]. This method provides a high-accuracy semianalytical solution of the Navier-Stokes and Poisson equations when the viscosity is only depth (radially) dependent (e.g., *Richard et al.* [1984], *Richards and Hager* [1984], *Forte and Peltier* [1987], *Corrieu et al.* [1994], *Forte and Perry* [2011], *Steinberger and Torsvik* [2008], and many others). However, the viscosity distribution in the Earth is essentially three-dimensional. In this case, the nonlinear coupling of different spherical harmonic modes does not allow obtaining a straightforward semianalytical solution. Several techniques have been suggested to account for LVV. Generally, most of them are based on an iterative approach proposed for such problems by *Orszag* [1971]. This method in application to LVV has been further developed by *Christensen and Harder* [1991] in the Cartesian domain. Later on, it was adapted for a spherical shell [*Zhang and Christensen*, 1993], and the iterative technique has been used in several studies [e.g., *Čadek and Fleitout*, 1999, 2003; *Karpychev and Fleitout*, 2000; *Kaban et al.*, 2007]. An alternative approach is to use a variational formulation of the buoyancy-driven mantle flow in a heterogeneous spherical shell solving the resulting system of equations by a direct method [e.g., *Moucha et al.*, 2007], or to use spatial domain methods [e.g., *Zhong et al.*, 2000].

[3] However, various studies using different numerical methods demonstrate inconsistent results for the calculated dynamic geoid, which is extremely sensitive to very small changes in the convecting flow pattern and associated changes in the dynamic topography. For example, *Martinec et al.* [1993], Zhang *and Christensen* [1993], *Forte and Peltier* [1994], and *Moucha et al.* [2007] conclude that LVV do not produce a significant effect on the geoid. At the same time, a number of other studies [e.g., *Zhong and Davies*, 1999; *Karpychev and Fleitout*, 2000; *Čadek and Fleitout*, 2003; *Kaban et al.*, 2007; *Ghosh et al.*, 2010] argue that their effect on the geoid is significant and may strongly influence the result of the geoid inversion.

[4] Owing to the controversial conclusions of existing studies, the problem of quantifying the effects of LVV in the mantle on the geoid calls for a comprehensive investigation. Several principal issues should be resolved. First of all, the existing techniques do not efficiently work in case of strong and high-gradient viscosity variations, which are typical for the Earth's mantle (more than 3 orders of magnitude in adjacent elements) [e.g., *Tackley*, 2008; *Deubelbeiss and Kaus*, 2008; *Furuichi et al.*, 2011]. Furthermore, increasing the spatial resolution leads to instabilities in the vicinity of the poles if spectral methods are used [e.g., *Holmes and Featherstone*, 2002]. Finally, it was recently shown [*Trubitsyn et al.*, 2008; *Rogozhina*, 2008] that the equations presented by *Zhang and Christensen* [1993] contain a number of typos that make it hard to reproduce their results.

[5] In this study, we present a numerical approach built up on the substantially revised method of *Zhang and Christensen* [1993], for solving the Navier-Stokes equations in the spectral domain with strong LVV. We suggest several algorithms, which provide efficient calculations of the instantaneous Stokes flow taking into account the effects of LVV, self gravitation, and compressibility. In particular, the Newton-Raphson procedure applied to the shooting method demonstrates the ability to solve the boundary value problem, necessary for cross-linking solutions on the sphere. In contrast to the traditionally used propagator method, our approach suggests continuous integration over depth. The Clenshaw-based recursion algorithms for computing associated Legendre functions and Horner's scheme for computing partial sums allow avoiding numerical instabilities in the vicinity of the poles, which are typical for the spherical harmonic method, and thus obtaining a fast and robust solution on the sphere for high degree and order. Some of the spherical harmonic transformation subroutines were developed using the freely available software SHTOOLS [*Wieczorek*, 2012]. The reliability and efficiency of the proposed technique is demonstrated by several benchmark tests.

# 2. Method

## 2.1. Governing Equations

[6] Our formulation for instantaneous viscous mantle flow in a spherical shell assumes compressibility, the 3-D distributions of viscosity $\eta = \eta(r, \theta, \varphi)$, density $\overline{\rho} = \rho(r) + \delta\rho(r, \theta, \varphi)$, and the effect of self gravitation. Under this formulation, the conservation equations of mass, momentum, and gravitational field flux in spherical coordinates are:

$$\frac{2u_r}{r} + \frac{\partial u_r}{\partial r} + \frac{1}{r}\left(\frac{\partial u_\theta}{\partial \theta} + \text{ctg}\theta u_\theta + \frac{1}{\sin\theta}\frac{\partial u_\varphi}{\partial \varphi}\right) = -\frac{k(r)}{r}u_r; \quad (1)$$

$$0 = -\frac{\partial p}{\partial r} + \frac{\partial \tau_{rr}}{\partial r} + \frac{1}{r}\frac{\partial \tau_{r\theta}}{\partial \theta} + \frac{1}{r\sin\theta}\frac{\partial \tau_{r\varphi}}{\partial \varphi}$$
$$+ \frac{1}{r}\left(2\sigma_{rr} - \sigma_{\theta\theta} - \sigma_{\varphi\varphi} + \tau_{r\theta}\mathrm{ctg}\theta\right) - \delta\rho g + \rho(r)\frac{\partial V}{\partial r} \quad (2)$$

$$0 = -\frac{1}{r}\frac{\partial p}{\partial \theta} + \frac{\partial \tau_{r\theta}}{\partial r} + \frac{1}{r}\frac{\partial \tau_{\theta\theta}}{\partial \theta} + \frac{1}{r\sin\theta}\frac{\partial \tau_{\theta\varphi}}{\partial \varphi}$$
$$+ \frac{1}{r}\left(\sigma_{\theta\theta}\mathrm{ctg}\theta - \sigma_{\varphi\varphi}\mathrm{ctg}\theta + 3\tau_{r\theta}\right) + \frac{\rho(r)}{r}\frac{\partial V}{\partial \theta} \quad (3)$$

$$0 = -\frac{1}{r\sin\theta}\frac{\partial p}{\partial \varphi} + \frac{\partial \tau_{r\varphi}}{\partial r} + \frac{1}{r}\frac{\partial \tau_{\theta\varphi}}{\partial \theta} + \frac{1}{r\sin\theta}\frac{\partial \tau_{\varphi\varphi}}{\partial \varphi}$$
$$+ \frac{1}{r}\left(3\tau_{r\varphi} + 2\tau_{\theta\varphi}\mathrm{ctg}\theta\right) + \frac{\rho(r)}{r\sin\theta}\frac{\partial V}{\partial \varphi} \quad (4)$$

$$\frac{\partial^2 V}{\partial r^2} + \frac{2}{r}\frac{\partial V}{\partial r} - \frac{L^2}{r}V = -4\pi\rho G,$$
$$L^2 = -\frac{1}{\sin\theta}\frac{\partial\left(\sin\theta\frac{\partial V}{\partial \theta}\right)}{\partial \theta} - \frac{1}{\sin^2\theta}\frac{\partial^2 V}{\partial \theta^2} \quad (5)$$

where $V$ is the gravitational potential, $G$ the gravitational constant, $g = g(r)$ is the gravitational acceleration, $k(r) = \frac{d\ln\rho(r)}{d\ln r}$ is the radial compressibility term [*Thoraval et al.*, 1994], and $(u_r, u_\theta, u_\varphi)$ is the velocity vector. The stress tensor $\sigma_{ij}$ can be expressed as the sum of the stress deviator $\tau_{ij}$ and pressure $p$: $\sigma_{ij} = \tau_{ij} - p\delta_{ij}$, where $\delta_{ij}$ is the unit tensor.

## 2.2. Numerical Method

[7] An iterative technique incorporating nonlinear terms in the form of corrections to the solution of the system of linear equations calculated in a collocated mesh was first proposed by *Orszag* [1971] and applied for the case of LVV in Cartesian [*Christensen and Harder*, 1991] and spherical [*Zhang and Christensen*, 1993] domains. In our approach, we attempt to further develop the method proposed by *Zhang and Christensen* [1993] to overcome a number of the problems associated with solving the Stokes equations in the spectral domain with strong LVV, which are mentioned in the introductory part.

[8] The solenoidal vector can be expressed as a sum of two independent fields: spheroidal and toroidal. In this case, the radial component of the solenoidal vector can be represented by a set of spherical harmonic functions $Y_{lm}(\theta, \varphi)$, whereas the lateral components are combinations of derivatives of the spherical harmonic function, $Y^\theta_{lm}(\theta, \varphi) = \frac{\partial Y_{lm}(\theta,\varphi)}{\partial \theta}$ and $Y^\varphi_{lm}(\theta, \varphi) = \frac{1}{\sin\theta}\frac{\partial Y_{lm}(\theta,\varphi)}{\partial \varphi}$.

[9] Assuming that the spherical harmonics are orthogonal over both $l$ and $m$ with the standard ge-

odesy normalization $\int_\Omega Y_{lm}(\Omega)Y_{l'm'}(\Omega) \ d\Omega = 4\pi\delta_{ll'} \ \delta_{mm'}$, we can express all the variables in equations (1)–(5) as follows:

$$u_r(r,\theta,\varphi) = \sum_{l,m} U_1^{lm}(r)Y_{lm}(\theta,\varphi)$$
$$u_\theta(r,\theta,\varphi) = \sum_{l,m}\left(U_2^{lm}(r)Y^\theta_{lm}(\theta,\varphi) + U_7^{lm}Y^\varphi_{lm}(\theta,\varphi)\right),$$
$$u_\varphi(r,\theta,\varphi) = \sum_{l,m}\left(U_2^{lm}(r)Y^\varphi_{lm}(\theta,\varphi) - U_7^{lm}Y^\theta_{lm}(\theta,\varphi)\right),$$
$$\sigma_{rr}(r,\theta,\varphi) = \frac{1}{r}\sum_{l,m}U_3^{lm}(r)Y_{lm}(\theta,\varphi),$$
$$\tau_{r\theta}(r,\theta,\varphi) = \frac{1}{r}\sum_{l,m}\left(U_4^{lm}(r)Y^\theta_{lm}(\theta,\varphi) + U_8^{lm}Y^\varphi_{lm}(\theta,\varphi)\right),$$
$$\tau_{r\varphi}(r,\theta,\varphi) = \frac{1}{r}\sum_{l,m}\left(U_4^{lm}(r)Y^\varphi_{lm}(\theta,\varphi) - U_8^{lm}Y^\theta_{lm}(\theta,\varphi)\right),$$
$$V(r,\theta,\varphi) = \sum_{l,m}U_5^{lm}(r)Y_{lm}(\theta,\varphi);$$
$$g(r,\theta,\varphi) = \nabla V = \sum_{l,m}U_6^{lm}(r)Y_{lm}(\theta,\varphi),$$
$$p(r,\theta,\varphi) = \sum_{l,m}p_{lm}(r)Y_{lm}(\theta,\varphi),$$
$$\delta p(r,\theta,\varphi) = \sum_{l,m}\delta\rho^{lm}Y_{lm}(\theta,\varphi),$$

$$(6)$$

where $U_1^{lm} - U_8^{lm}$ depend on radius. The terms $U_1^{lm} - U_4^{lm}$ are the poloidal, and $U_7^{lm}, U_8^{lm}$ are the toroidal components of the velocity and stress fields. The stress tensor components, $\tau_{\theta\theta}$, $\tau_{\varphi\varphi}$, and $\tau_{\theta\varphi}$, can then be expressed in terms of the velocity vector components, $u_r$, $u_\theta$, and $u_\varphi$. Substituting the above relations (6) into equations (1)–(5) and projecting the equations onto corresponding spherical harmonics [e.g., *Zhang and Christensen*, 1993; *Trubitsyn et al.*, 2008; *Rogozhina*, 2008], we arrive at the following set of equations:

$$\frac{1}{r}\frac{dU_1^{lm}}{dr} = -(2+k)U_1^{lm} + LU_2^{lm} + A^{lm} \quad (7)$$

$$\frac{1}{r}\frac{dU_2^{lm}}{dr} = -U_1^{lm} + U_2^{lm} + \frac{1}{\eta^*}U_4^{lm} + B^{lm} \quad (8)$$

$$\frac{1}{r}\frac{dU_3^{lm}}{dr} = (12+4k)\eta^*U_1^{lm} - 6L\eta^*U_2^{lm} + U_3^{lm} + LU_4^{lm}$$
$$+ (1+k)\rho^*U_5^{lm} + \delta\rho^{lm}g^* + C^{lm} \quad (9)$$

$$\frac{1}{r}\frac{dU_4^{lm}}{dr} = -(6+2k)\eta^*U_1^{lm} + 2(2L-1)\eta^*U_2^{lm}$$
$$- U_3^{lm} - 2U_4^{lm} + D^{lm} \quad (10)$$

$$\frac{1}{r}\frac{dU_5^{lm}}{dr} = U_5^{lm} + U_6^{lm} \quad (11)$$

$$\frac{1}{r}\frac{dU_6^{lm}}{dr} = LU_5^{lm} - 4\pi G\delta\rho^{lm}R\rho_0 r^3/g_0 \quad (12)$$

$$\frac{1}{r}\frac{dU_7^{lm}}{dr} = U_7^{lm} + \frac{1}{\eta^*}U_8^{lm} + E^{lm} \qquad (13)$$

$$\frac{1}{r}\frac{dU_8^{lm}}{dr} = (L-2)\eta^* U_7^{lm} - 2U_8^{lm} + F^{lm} \qquad (14)$$

where $\rho^* = \rho(r)/\rho_0$ and $\eta^* = \eta(r)/\eta_0$ are the normalized radial density and viscosity, $\rho_0$ and $\eta_0$ are the reference mantle density and viscosity, $g_0$ is the gravity acceleration at the surface, $G$ is the gravitational constant, $R$ is the Earth's radius, and $L = l(l+1)$. The vector $S^{lm} = \left(A^{lm}, B^{lm}, C^{lm}, D^{lm}, E^{lm}, F^{lm}\right)$ is the viscous loading term that accounts for the effects of LVV (see Appendix A). Note that for $l = 1$, singularity of the system of equations (7)–(14) appears (see equation (14)). To avoid this, we assume the no-net rotation reference frame for the toroidal component $\left(U_7^{1m} = 0\right)$ that is similar to the condition used by *Zhang and Christensen* [1993]. The equations (7)–(14) are complemented by following boundary conditions:

$$U_1^{lm}(r_e, r_c) = U_4^{lm}(r_e, r_c) = U_8^{lm}(r_e, r_c) = 0 \qquad (15)$$

(free-slip conditions at the Earth's surface and the core-mantle boundary (CMB)

$$U_6^{lm}(r_e) = -(l+1)U_5^{lm}(r_e) - \frac{4\pi GR\rho_0}{g_e}\left(U_3^{lm}(r_e) - \rho^* U_5^{lm}(r_e)\right) \qquad (16)$$

$$\begin{aligned}U_6^{lm}(r_c) = &\,(l-3)U_5^{lm}(r_c)\\ &- \frac{4\pi GR_{CMB}\rho_0}{g_c}\left(U_3^{lm}(r_c) - \rho^* U_5^{lm}(r_c)\right)\end{aligned} \qquad (17)$$

where $R_{CMB}$ is the radius of the CMB; $r_c$ and $r_e$ are the normalized radius of the CMB and Earth's surface, respectively.

[10] Integration in the radial direction is performed by a finite difference method in contrast to the traditionally used propagator matrix method. This approach allows operating with continuous physical properties and avoiding problems with artificial stress discontinuities, which are revealed by *Corrieu et al.* [1995] in case of a compressible mantle. Since our method implies a nonuniform spatial discretization by radius, any discontinuity in physical parameters (such as abrupt changes in density or radial viscosity) can be resolved using a mesh refinement. To advance the solution from the initial point $r$ to the point $r + H$, where H is a given spatial step, we use the modified midpoint method [e.g., *Press et al.*, 2007, p. 923]. We solve the two-point boundary value problem using the shooting method and the two-step Newton-Raphson procedure. Since the spectral methods are extremely sensitive to rounding errors, especially for high orders [e.g., *Trefethen and Trummer*, 1987], the second step might be necessary to reduce the round-off errors. We use the solution obtained at the first step as an initial guess for the second step. However, this method becomes unstable under relatively high spherical harmonics ($l > 60$). This instability increases in the direction of integration if the shooting method is used. Therefore, the boundary value problem is solved two times by integrating in opposite directions. If the stable part of the solution overlaps, we can compile the final solution for every degree and order (see Figure S1, supporting information).[1] This obvious trick enhances stability of the solution up to the degree/order of 180. In our tests, we have found that the stability depends on density and viscosity structure of particular models and the maximum resolution may be from 100 to 180. The method requires using at least the double-precision floating-point format for real numbers to achieve such resolution.

[11] The Clenshaw-based recursion algorithm for computing the associated Legendre functions and the Horner's scheme for computing partial sums allow avoiding the problems in the vicinity of the poles, which are typical for spherical harmonic methods, and obtaining a fast and robust solution on the sphere for high degree and order [*Holmes and Featherstone*, 2002; *Wieczorek*, 2012]. Differentiation of the functions on the sphere (e.g., second derivatives of strain necessary for the viscous loading terms) is performed in a space domain on the Gauss-Legendre quadrature nodes. A comparative analysis has shown that this method provides more precise and noise-free results than the differentiation in a spectral domain, especially at high orders and in the vicinity of the poles.

[12] A fixed-point iteration method is used to obtain values of the viscous loading vector $S^{lm}$. Initially, the vector components are set to zero; therefore, the initial solution is computed assuming a radial distribution of viscosity. Then, the viscous loading vector is calculated based on the solution obtained from the previous iteration step. In case of relatively small LVV, the algorithm converges fast and steadily. However, when the LVV are large (more than 2 orders of magnitude) some additional stabilizing procedures must be

---

[1]Additional supporting information may be found in the online version of this article.

applied. To stabilize and enhance convergence of the method, the following simple under-relaxation scheme for the viscous loading vector is applied:

$$\overline{S}_i^{lm} = (1 - \lambda)S_{i-1}^{lm} + \lambda S_i^{lm}, \qquad 0 \leq \lambda \leq 1 \qquad (18)$$

where $i$ is the number of iteration. In general, the value of the stabilizing term $\lambda$ is inversely proportional to the LVV magnitude. Initially, $\lambda = 0.5$, then it is reduced automatically if the method fails to converge. The radial viscosity $\eta(r)$ is chosen as the minimal viscosity at each depth. Numerical tests have demonstrated that the use of alternative reference radial viscosity (e.g., average or log mean average) leads to inaccurate solutions in benchmark tests with strong LVV (especially for low-viscosity zones). Even though with large LVV this approach slows down the convergence, it provides a good conformity with theoretical solutions in benchmark tests.

[13] The described algorithms have been integrated in the "ProSpher" code, which is tested below.

## 3. Benchmarks

[14] Since benchmarking techniques for 3-D spherical codes are not well established, we employ different approaches to test the method developed. First, we show that the algorithm gives a correct result for a radially symmetric viscosity distribution. Second, an iterative scheme for the LVV case is validated by comparing the solution for a tetrahedral symmetric ($l = 3$, $m = 2$) steady state compressible convective flow, comprising temperature-dependent Newtonian viscosity, with the solution obtained from the CitcomS numerical code [*Zhong et al.*, 2000; *Tan et al.*, 2006] for the same problem. In the supporting information (Text S1), we analyze the applicability of the technique to different LVV patterns and various viscosity contrasts.

### 3.1. Radial Viscosity Case

[15] First, we test the consistency of both the ProSpher and CitcomS codes for the model with radial viscosity changes only. Without LVV, the system of equations (7)–(12) is reduced to the form obtained by *Thoraval et al.* [1994] and *Corrieu et al.* [1995] that provides the possibility for an exact semianalytical solution. Comparison of the results obtained from the ProSpher code with those

obtained from the propagator method and the alternative "direct integration" method of *Kaban et al.* [2007] shows their full correspondence. To compare the ProSpher and CitcomS codes, we use the solution of the Cookbook 1 example [*Tan et al.*, 2012] obtained from the CitcomS. Despite the fact that the benchmark is widely used in many studies [e.g., *Ratcliff et al.*, 1996; *Zhong et al.*, 2000; *Yoshida and Kageyama*, 2004; *Stemmer et al.*, 2006], we refer to the CitcomS user guide [*Tan et al.*, 2012] since it provides a detailed description and all necessary input files for the use of the CitcomS. For the temperature field that initially has tetrahedral symmetric ($l = 3$, $m = 2$) perturbation, we find a steady state solution. The final density distribution is then used for calculation of the instantaneous mantle flow by the means of the ProSpher code. After corresponding scaling is applied, we get the result that agrees well with the results from the CitcomS, within of less than 0.5% root-mean-square velocity (Vrms). Such degree of agreement between independent methods confirms the reliability of the ProSpher code to calculate the poloidal flow components and corresponding fields.

### 3.2. Compressible Mantle Flow With LVV

[16] In order to test full functionality of the ProSpher code, we perform a comparative test for a compressible thermal convection (CitcomS Cookbook 8 example [*Tan et al.*, 2012]), which is often used for comparison with other methods [e.g., *Ratcliff et al.*, 1996; *Richards et al.*, 2001; *Yoshida and Kageyama*, 2004; *Zhong et al.*, 2008]. The setup is basically similar to that described in section 3.1 but now with a 3-D temperature-dependent viscosity. The 3-D density and viscosity distributions obtained from the CitcomS steady state solution are used to calculate the instantaneous velocity field by the ProSpher code. We have obtained a reasonably good correspondence between the modeled velocity fields within 3% Vrms (Figure 1, mean Vrms of 26.58 versus 27.36 by CitcomS [*Zhong et al.*, 2008]) and less than 1% Vrms as compared with *Ratcliff et al.* [1996] (mean Vrms = 26.8)

### 3.3. "Half-sphere" Test

[17] It is known that sharp and large viscosity contrasts in a model may lead to numerical instabilities and consequently to problems with the method convergence. To test the ability of the ProSpher code to handle such viscosity contrasts, we have developed a new "stress" test. The idea
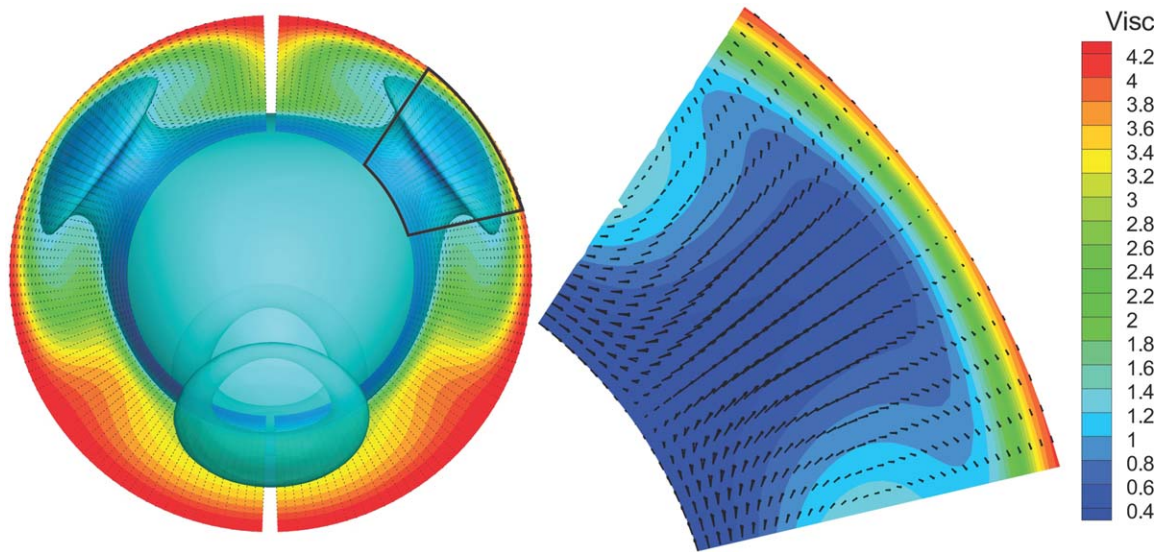
**Figure 1.** Viscosity distribution in a compressible steady state convection problem (see text, section 3.2). (left) The viscosity isosurface of 1 is shown. (right) The resulting velocity fields from the CitcomS and ProSpher codes are shown as superimposed vector fields.

of this benchmark problem is based on the fact that the velocity of a body with negative (or positive) buoyancy is inversely proportional to the viscosity of surrounding medium, as follows from the Stokes' law if the Reynolds number is small. The sphere is divided into two hemispheres. Two identical bodies with negative buoyancy are placed in the center of each hemisphere (Figure 2a). In each experiment, the viscosity in one hemisphere (right hemisphere in Figure 2a) remains constant (reference hemisphere), while the viscosity in the other hemisphere is varied.

[18] In our tests, we employ a lateral resolution of 60 spherical harmonics and 100 km by radius. The

size of each body is $1000 \times 1000 \times 500$ km. Normalized by its maximum value, the velocity depends only on the viscosity contrast between two hemispheres. The result is presented in Figure 3. The test demonstrates convergence of the method for the viscosity contrasts up to 3 orders of magnitude for this particular geometry. Further analysis shows that, although it is possible to obtain the correct solution for velocity of sinking bodies with higher viscosity contrasts (up to $10^5$), it is hardly possible to achieve the required accuracy (0.01% for $\Delta$Vrms). Probably it is due to the numerical noise caused by round off errors [e.g., *Trefethen and Trummer*, 1987], which is compatible by
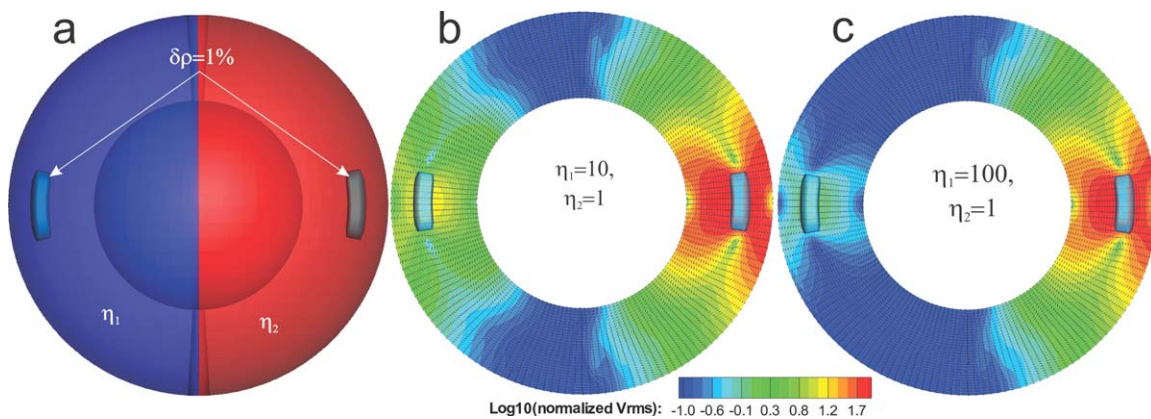


**Figure 2.** (a) Benchmark problem setup and modeling results for: (b) 1 order and (c) 2 orders of viscosity contrast magnitude. Arrows (at Figures 2b and 2c) indicate the directions of the fluid flow. Decimal logarithm of the normalized Vrms is shown in color.
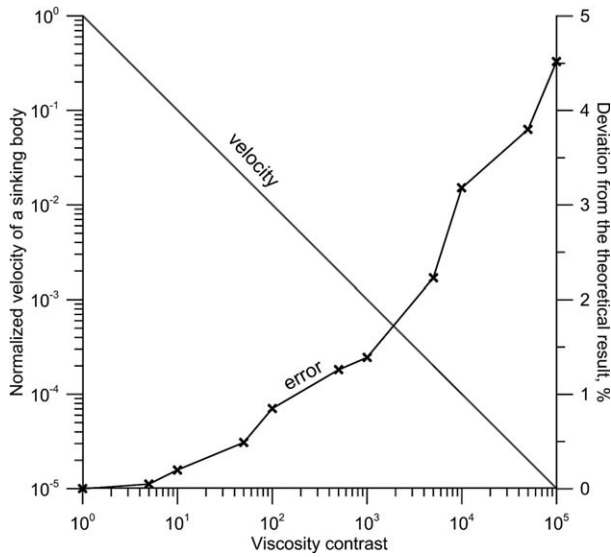
**Figure 3.** Velocity of the center of a sinking body placed in the low-viscosity hemisphere, normalized by the maximum velocity; and deviation from the theoretically estimated values for the velocity versus viscosity contrast between the two hemispheres.

amplitude to the solution for velocity in the hemisphere with lower viscosity in the areas far-off from the sinking body. The solution in the reference hemisphere remains correct for the considered values of LVV (up to 5 orders of magnitude).

[19] Implementation of spherical bodies in the model has some difficulties due to the limited. However, possible deviations from the requirements of the Stokes' law (see Figures 2b, 2c, and 3) do not affect remarkably the results, which are in a good agreement with the theoretical estimates.

## 4. Effects of LVV on the Geoid

[20] The observed geoid is an integral parameter that depends on both density variations within the Earth and LVV and is thus sensitive to the rheological structure of the mantle. Therefore, it is important to analyze effects of LVV on the geoid. In this paper, we do not intend to construct a self-consistent global model of the mantle, which would require a more extensive work on a joint interpretation of various fields. Here, we intend to demonstrate potential effects of LVV as estimated from seismic-tomography based 3-D viscosity models of the mantle and to test the ability of the code to handle high lateral viscosity contrast.

[21] Density variations are calculated using standard velocity-to-density scaling factor $\alpha = 0.2$

(equation (19)), which is generally consistent with the mineral physics estimations and previous studies [e.g., *Karato*, 1993; *Mitrovica and Forte*, 2004; *Steinberger and Calderwood*, 2006; *Kaban and Trubitsyn*, 2012]. These are applied to the S40RTS model [*Ritsema et al.*, 2011] as follows:

$$\delta\rho(r,\theta,\varphi) = \alpha \frac{\delta V_s(r,\theta,\varphi)}{V_s(r,\theta,\varphi)} \rho(r). \tag{19}$$

[22] The viscosity model is obtained using the homologous temperature approach [e.g., *Yamazaki and Karato*, 2001]. The homologous temperature is the ratio of the actual temperature to the melting point. Temperature variations $\delta T(r,\theta,\varphi)$ are derived from density anomalies by applying a depth-dependent thermal-expansion coefficient [e.g., *Paulson et al.*, 2005], which in combination with adiabatic temperature profile $T_a(r)$ [*Katsura et al.*, 2010] gives 3-D distribution of absolute temperature. Then, temperature variations are converted into viscosity variations as follows:

$$\eta(r,\theta,\varphi) = A_0(r)\exp\left(E\frac{T_m(r)}{T_a(r) + \delta T(r,\theta,\varphi)}\right). \tag{20}$$

[23] Depth-dependent melting temperature $T_m(r)$ is calculated as: $T_m(d) = 2100 + 1.4848d - 5 \times 10^{-4}d^2$) in the upper mantle and $T_m(d) = 2916 + 1.25d - 1.65 \times 10^{-4}d^2$) in the lower mantle, where $d$ is the depth in kilometers [*Yamazaki and Karato*, 2001], $r = 1 - d/R$, and $R$ is the Earth radius. The coefficient $E$ scales the amplitude of LVV. Within the range of LVV considered in this study, the maximal viscosity contrast ($E = 12$ reaches $\sim 5$ orders of magnitude within the uppermost mantle (Figures 5 and S2, supporting information). Such large contrasts cover the range of viscosity that is usually used in mantle convection models including slabs dipping in the mantle and the lithosphere heterogeneity [e.g., *Ghosh et al.*, 2010]. In order to keep the radial viscosity constant for any given value $E$, we calculate the coefficient $A_0$ as follows:

$$A_0(r) = \frac{\eta(r)}{\overline{\eta}(r)},$$

$$\log_{10}(\overline{\eta}(r)) = \frac{\sum_i^{N_\theta}\sum_j^{N_\varphi}\left[\log_{10}(\eta(r,\theta_i,\varphi_j)\cos(\theta_i)\right]}{N_\varphi\sum_i^{N_\theta}\cos(\theta_i)} \tag{21}$$

where $\overline{\eta}(r)$ is the mean viscosity weighted by the area, $N_\theta$ and $N_\varphi$ are the numbers of points by
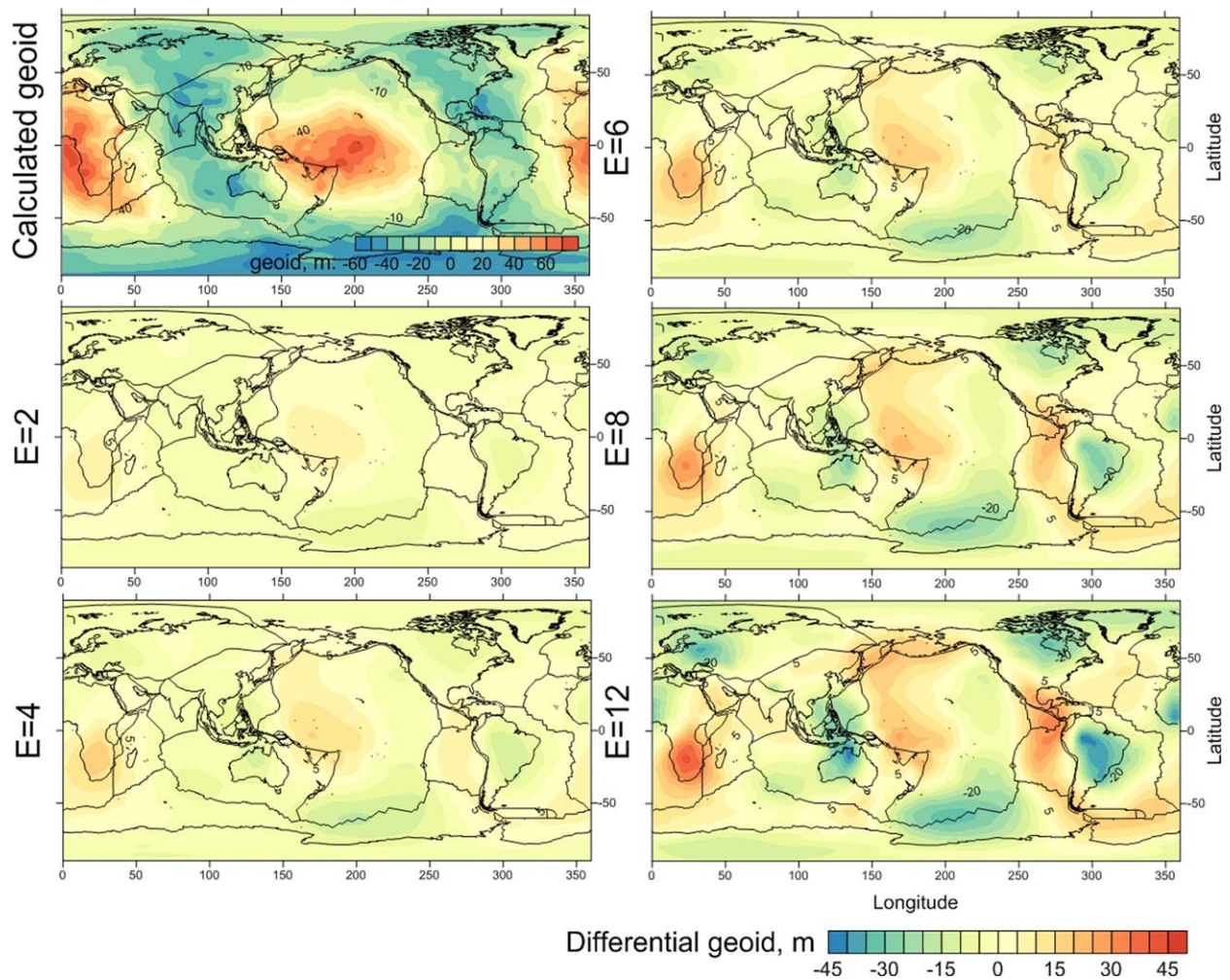
**Figure 4.** Perturbations of the dynamic geoid, induced by LVV, relative to the reference geoid (radial viscosity only, upper left, $E = 0$) for various amplitudes of LVV. The scaling coefficient E linearly modifies LVV from no- to full- LVV model. $E = 0$ corresponds to the no- LVV model (radial viscosity variations only), $E = 6$ gives 50% of the maximum LVV that corresponds to $E = 12$. The radial viscosity distribution and the bounds of the viscosity for $E = 6$ and $E = 12$ are presented in the supporting information, Figure S2.

latitude and longitude, respectively. The LVV can be expressed as follows:

$$\delta\eta(r, \theta, \varphi) = \eta(r, \theta, \varphi) - \eta(r) \qquad (22)$$

that in combination with the equations (20) and (21) gives the linear dependence of LVV on the coefficient $E$, while keeping the radial viscosity unchanged (Figure S3, supporting information). Using this approach, we can thus assess the pure influence of LVV on the modeled geoid.

[24] By increasing the LVV range, several areas are revealed where LVV most significantly influence the geoid. The strongest negative perturbations in the dynamic geoid, induced by LVV, are found around Northern Australia and in the central part of South America, 42 and 44 m, respectively, for $E = 12$, Figure 4. Prominent negative anomalies also appear in Southern Pacific, Northern America, Eastern Europe and North-West Africa. By contrast, the South African and Eastern Pacific areas are characterized by positive perturbations in the geoid of 41 and 32 m, respectively. In general, North-West and South-East Pacific are characterized by positive perturbations in the dynamic geoid induced by LVV with the amplitude of 20 m on average. The modeling results demonstrate a close-to-linear relationship between the LVV-related geoid perturbations and LVV amplitude (Figure S4, supporting information).
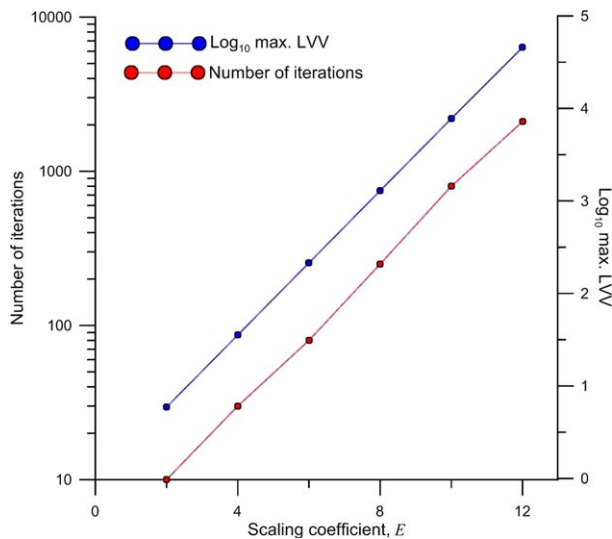
**Figure 5.** Convergence of the method versus maximum value of LVV that is defined by scaling coefficient $E$ according to equation (20).

[25] We repeat calculations using the alternative tomographic model [*Gu et al.*, 2003]. Although a resulting map of LVV-related geoid anomalies differs in some details from the map presented in Figure 4, the major features are reproduced by both simulations (Figure S5, supporting information).

[26] According to our results, the convergence rate of the method is proportional to the maximum LVV value (Figure 5). For instance, the solution of the problem with maximum LVV of 4 orders of magnitude takes about 15 min (~3000 iterative steps) using single thread on the Intel Core i7 3.2 GHz processor for the resolution of 40 spherical harmonics on the sphere, and ~50 km (58 elements) by radius that corresponds roughly to a spatial resolution of 500 km × 500 km × 50 km. The solution of the same problem with maximum LVV of 10 takes about 8 s (28 iterative steps).

## 5. Discussion and Conclusions

[27] Employing innovative algorithms, we have developed a powerful method for calculations of the instantaneous viscous flow in a sphere handling strong LVV (~5 orders of magnitudes), compressibility, and self gravitation. The ProSpher code enables predictive solutions with high resolution in both lateral (up to a spherical harmonic degree and order of 180) and radial (about 20 km by depth) directions showing a high computational

efficiency. However, this code has some limitations inherited from spectral methods such as round-off errors and aliasing. The method requires using at least the double-precision floating-point format for real numbers. Further increase in accuracy (12 or 16 bit for real numbers) will improve stability of the method under high resolution (120 spherical harmonics and more) but will also increase a computational time. We assume that the use of the relaxation method instead of (or in combination with) the shooting method, applied to integration in the radial direction, can also improve the stability of the code if higher resolution is necessary. The under-relaxation iterative algorithm, which we use in the ProSpher code, shows direct dependence of the convergence rate on maximum LVV, i.e., it takes approximately 10–30 iterative steps for maximum LVV of 10 and ~$10^5$ iterative steps for LVV of $10^5$ to achieve a 0.01% $\Delta$Vrms tolerance.

[28] A number of benchmarks have demonstrated a good agreement between the results of simulations and theoretical estimates. We have also developed a simple benchmark for a quantitative testing of viscous flow simulations (the "half-sphere" test, see section 3.3). Based on a number of benchmarks, we have found that the choice of a radial reference viscosity is essential. Correct results were only obtained when the reference viscosity corresponds to the minimal value at each depth. Although such a choice slows down convergence of the iterative adjustment, any other choice (e.g., average or log-mean average as suggested by previous studies) leads to incorrect solutions for the simulations with strong LVV and especially in low-viscosity zones.

[29] Our tests confirm that the effect of LVV on the geoid is significant, as has been shown by earlier studies [e.g., *Karpychev and Fleitout*, 2000; *Kaban et al.*, 2007; *Ghosh et al.*, 2010]. Maximum deviations from the reference geoid calculated for the case of only radial viscosity variations in the mantle amount to about ±40 m as derived from the model with maximum LVV (about 5 orders of magnitudes using the tomographic model S40RTS). These values are comparable with amplitudes of the reference geoid (−56 m, +76 m). Thus, we can conclude that strong LVV and the choice of a radial viscosity distribution exert a strong influence on the mantle dynamics. The results of the simulations reveal a high potential of the ProSpher code which can be efficiently used for solution of the mantle flow problems.

# Appendix A: The Components of the Vector $S^{lm}$

[30]

$$S^{lm} = \left( A^{lm}, B^{lm}, C^{lm}, D^{lm}, E^{lm}, F^{lm} \right)$$

$$A^{lm} = 0$$

$$B^{lm} = -\frac{2r}{s_{lm}\eta^*} \int_0^{2\pi} d\varphi \int_0^{\pi} \tilde{\eta} \left( e_{r\theta} Y_{lm}^{\theta} + e_{r\varphi} Y_{lm}^{\varphi} \right) \sin\theta d\theta$$

$$C^{lm} = -\frac{6r}{s_{m0}} \int_0^{2\pi} d\varphi \int_0^{\pi} \tilde{\eta} \left( e_{rr} + \frac{k(r)}{3r} u_r \right) Y_{lm} \sin\theta d\theta$$

$$D^{lm} = -\frac{2r^2}{s_{lm}} \int_0^{2\pi} d\varphi \int_0^{\pi} \left( D_\theta Y_{lm}^{\theta} + D_\varphi Y_{lm}^{\varphi} \right) \sin\theta d\theta - \frac{1}{3} C^{lm}$$

$$E^{lm} = -\frac{2r}{s_{lm}\eta^*} \int_0^{2\pi} d\varphi \int_0^{\pi} \tilde{\eta} \left( e_{r\theta} Y_{lm}^{\varphi} - e_{r\varphi} Y_{lm}^{\theta} \right) \sin\theta d\theta$$

$$F^{lm} = -\frac{2r^2}{s_{lm}} \int_0^{2\pi} d\varphi \int_0^{\pi} \left( D_\theta Y_{lm}^{\varphi} - D_\varphi Y_{lm}^{\theta} \right) \sin\theta d\theta$$

where $e_{ij}$ are the components of the strain tensor, $s_{m0} = 4\pi$, $s_{lm} = s_{m0} l(l+1)$

$$D_\theta = \frac{1}{r^2} \left[ \frac{\partial \left( r\tilde{\eta} e_{\theta\theta} + \frac{k(r)}{3}\tilde{\eta} u_r \right)}{\partial\theta} + r\tilde{\eta}\left(e_{\theta\theta} - e_{\varphi\varphi}\right)\text{ctg}\theta + \frac{r}{\sin\theta}\frac{\partial\left(\tilde{\eta} e_{\theta\varphi}\right)}{\partial\varphi} \right]$$

$$D_\varphi = \frac{1}{r^2} \left[ \frac{1}{\sin\theta}\frac{\partial \left( r\tilde{\eta} e_{\varphi\varphi} + \frac{k(r)}{3}\tilde{\eta} u_r \right)}{\partial\varphi} + 2r\tilde{\eta} e_{\theta\varphi}\text{ctg}\theta + r\frac{\partial\left(\tilde{\eta} e_{\theta\varphi}\right)}{\partial\theta} \right]$$

[31]  Velocity scaling (result is in m/s):

$$u(r,\theta,\varphi)_{real} = u(r,\theta,\varphi)_{calc} \frac{R^2 g_0 \rho_0}{\eta_0}.$$

# Acknowledgments

# References

Čadek, O., and L. Fleitout (1999), A global geoid model with imposed plate velocities and partial layering, *J. Geophys. Res.*, *104*(B12), 29,055–29,075, doi:10.1029/1999JB900150.

Čadek, O., and L. Fleitout (2003), Effect of lateral viscosity variations in the top 300 km on the geoid and dynamic topography, *Geophys. J. Int.*, *152*(3), 566–580, doi:10.1046/j.1365-246X.2003.01859.x.

Christensen, U., and H. Harder (1991), 3-D convection with variable viscosity, *Geophys. J. Int.*, *104*(1), 213–220, doi:10.1111/j.1365-246X.1991.tb02505.x.

Corrieu, V., Y. Ricard, and C. Froidevaux (1994), Converting mantle tomography into mass anomalies to predict the Earth's radial viscosity, *Phys. Earth Planet. Inter.*, *84*(1-4), 3–13, doi:10.1016/0031-9201(94)90031-0.

Corrieu, V., C. Thoraval, and Y. Ricard (1995), Mantle dynamics and geoid Green functions, *Geophys. J. Int.*, *120*(2), 516–523, doi:10.1111/j.1365-246X.1995.tb01835.x.

Deubelbeiss, Y., and B. J. P. Kaus (2008), Comparison of Eulerian and Lagrangian numerical techniques for the Stokes equations in the presence of strongly varying viscosity, *Phys. Earth Planet. Inter.*, *171*(1–4), 92–111, doi:10.1016/j.pepi.2008.06.023.

Forte, A. M., and W. R. Peltier (1987), Plate tectonics and aspherical earth structure: The importance of poloidal-toroidal coupling, *J. Geophys. Res.*, *92*(B5), 3645–3679, doi:10.1029/JB092iB05p03645.

Forte, A. M., and W. R. Peltier (1994), *The kinematics and dynamics of poloidal-toroidal coupling in mantle flow: The importance of surface plates and lateral viscosity variations*, vol. *36*, edited by R. Dmowska and B. Saltzman, pp. 1–119, Academic, San Diego, Calif.

Forte, A. M., and H. K. C. Perry (2000), Geodynamic evidence for a chemically depleted continental tectosphere, *Science*, *290*(5498), 1940–1944.

Furuichi, M., D. A. May, and P. J. Tackley (2011), Development of a Stokes flow solver robust to large viscosity jumps using a Schur complement approach with mixed precision arithmetic, *J. Comput. Phys.*, *230*(24), 8835–8851, doi:10.1016/j.jcp.2011.09.007.

Ghosh, A., T. W. Becker, and S. J. Zhong (2010), Effects of lateral viscosity variations on the geoid, *Geophys. Res. Lett.*, *37*, L01301, doi:10.1029/2009GL040426.

Gu, Y. J., A. M. Dziewoński, and G. Ekström (2003), Simultaneous inversion for mantle shear velocity and topography of

transition zone discontinuities, *Geophys. J. Int.*, *154*(2), 559–583, doi:10.1046/j.1365-246X.2003.01967.x.

Hager, B. H., and R. J. O'Connell (1981), A simple global model of plate dynamics and mantle convection, *J. Geophys. Res.*, *86*(B6), 4843–4867, doi:10.1029/JB086iB06p04843.

Holmes, S. A., and W. E. Featherstone (2002), A unified approach to the Clenshaw summation and the recursive computation of very high degree and order normalised associated Legendre functions, *J. Geod.*, *76*(5), 279–299.

Kaban, M. K., and V. Trubitsyn (2012), Density structure of the mantle transition zone and the dynamic geoid, *J. Geodyn.*, *59-60*, 183–192, doi:10.1016/j.jog.2012.02.007.

Kaban, M. K., I. Rogozhina, and V. Trubitsyn (2007), Importance of lateral viscosity variations in the whole mantle for modelling of the dynamic geoid and surface velocities, *J. Geodyn.*, *43*(2), 262–273.

Karato, S. (1993), Importance of anelasticity in the interpretation of seismic tomography, *Geophys. Res. Lett.*, *20*(15), 1623–1626, doi:10.1029/93GL01767.

Karpychev, M., and L. Fleitout (2000), Long-wavelength geoid: The effect of continental roots and lithosphere thickness variations, *Geophys. J. Int.*, *143*(3), 945–963, doi:10.1046/j.1365-246X.2000.00309.x.

Katsura, T., A. Yoneda, D. Yamazaki, T. Yoshino, and E. Ito (2010), Adiabatic temperature profile in the mantle, *Phys. Earth Planet. Inter.*, *183*(1-2), 212–218, doi:10.1016/j.pepi.2010.07.001.

Martinec, Z., C. Matyska, O. Čadek, and P. Hrdina (1993), The stokes problem with 3D Newtonian rheology in a spherical shell, *Comput. Phys. Commun.*, *76*(1), 63–79, doi:10.1016/0010–4655(93)90121-R.

Mitrovica, J. X., and A. M. Forte (2004), A new inference of mantle viscosity based upon joint inversion of convection and glacial isostatic adjustment data, *Earth Planet. Sci. Lett.*, *225*(1-2), 177–189, doi:10.1016/j.epsl.2004.06.005.

Moucha, R., A. M. Forte, J. X. Mitrovica, and A. Daradich (2007), Lateral variations in mantle rheology: Implications for convection related surface observables and inferred viscosity models, *Geophys. J. Int.*, *169*(1), 113–135, doi:10.1111/j.1365-246X.2006.03225.x.

Orszag, S. A. (1971), Numerical simulation of incompressible flows within simple boundaries: Accuracy, *J. Fluid Mech.*, *49*(01), 75–112.

Paulson, A., S. Zhong, and J. Wahr (2005), Modelling postglacial rebound with lateral viscosity variations, *Geophys. J. Int.*, *163*(1), 357–371, doi:10.1111/j.1365-246X.2005.02645.x.

Press, W. H., S. A. Teukolsky, W. T. Vetterling, and B. P. Flannery (2007), *Numerical Recipes: The Art of Scientific Computing*, 3rd ed., Cambridge Univ. Press., New York, NY 10013–2473, USA.

Ratcliff, J. T., G. Schubert, and A. Zebib (1996), Steady tetrahedral and cubic patterns of spherical shell convection with temperature-dependent viscosity, *J. Geophys. Res.*, *101*(B11), 25,473–25,484, doi:10.1029/96JB02097.

Richard, Y. L., L. Fleitout, and C. Froidevaux (1984), Geoid heights and lithospheric stresses for a dynamical Earth, *Ann. Geophys.*, *2*, 267–286.

Richards, M. A., and B. H. Hager (1984), Geoid anomalies in a dynamic earth, *J. Geophys. Res.*, *89*(B7), 5987–6002, doi:10.1029/JB089iB07p05987.

Richards, M. A., W. S. Yang, J. R. Baumgardner, and H. P. Bunge (2001), Role of a low-viscosity zone in stabilizing plate tectonics: Implications for comparative terrestrial planetology, *Geochem. Geophys. Geosyst*, *2*(8), 1026.

Ritsema, J., A. Deuss, H. J. van Heijst, and J. H. Woodhouse (2011), S40RTS: A degree-40 shear-velocity model for the mantle from new Rayleigh wave dispersion, teleseismic traveltime and normal-mode splitting function measurements, *Geophys. J. Int.*, *184*(3), 1223–1236, doi:10.1111/j.1365-246X.2010.04884.x.

Rogozhina, I. (2008), Global modeling of the effect of strong lateral viscosity variations on dynamic geoid and mantle flow velocities, Sci. Tech. Rep. STR08/08, Dtsch. GeoForschungsZentrum, Potsdam. [Available at http://www.gfz-potsdam.de/bib/pub/str0808/0808.pdf.].

Steinberger, B., and A. R. Calderwood (2006), Models of large-scale viscous flow in the Earth's mantle with constraints from mineral physics and surface observations, *Geophys. J. Int.*, *167*(3), 1461–1481, doi:10.1111/j.1365-246X.2006.03131.x.

Steinberger, B., and T. H. Torsvik (2008), Absolute plate motions and true polar wander in the absence of hotspot tracks, *Nature*, *452*(7187), 620–623, doi:10.1038/nature06824.

Stemmer, K., H. Harder, and U. Hansen (2006), A new method to simulate convection with strongly temperature- and pressure-dependent viscosity in a spherical shell: Applications to the Earth's mantle, *Phys. Earth Planet. Inter.*, *157*(3–4), 223–249, doi:10.1016/j.pepi.2006.04.007.

Tackley, P. J. (2008), Modelling compressible mantle convection with large viscosity contrasts in a three-dimensional spherical shell using the yin-yang grid, *Phys. Earth Planet. Inter.*, *171*(1-4), 7–18, doi:10.1016/j.pepi.2008.08.005.

Tan, E., E. Choi, P. Thoutireddy, M. Gurnis, and M. Aivazis (2006), GeoFramework: Coupling multiple models of mantle convection within a computational framework, *Geochem. Geophys. Geosyst.*, *7*, Q06001, doi:10.1029/2005GC001155.

Tan, E., M. Gurnis, L. Armendariz, L. Strand, and S. Kientz (2012), CitcomS, User Manual, Version 3.2.0., California Institute of Technology, Pasadena, Calif. [Available at http://www.geodynamics.org/cig/software/citcoms/citcoms.pdf.].

Thoraval, C., P. Machetel, and A. Cazenave (1994), Influence of mantle compressibility and ocean warping on dynamical models of the geoid, *Geophys. J. Int.*, *117*(2), 566–573, doi:10.1111/j.1365-246X.1994.tb03954.x.

Trefethen, L. N., and M. R. Trummer (1987), An instability phenomenon in spectral methods, *SIAM J. Numer. Anal.*, *24*(5), 1008–1023, doi:10.1137/0724066.

Trubitsyn, V. P., I. E. Rogozhina, and M. K. Kaban (2008), On a spectral method of solving the Stokes equation, Izvestiya, *Phys. Solid Earth*, *44*(1), 18–25.

Wieczorek, M., (2012) SHTOOLS, Tools for working with spherical harmonics. Institut de Physique du Globe de Paris, Paris, France [Available at http://shtools.ipgp.fr.]

Yamazaki, D., and S. Karato (2001), Some mineral physics constraints on the rheology and geothermal structure of Earth's lower mantle, *Am. Mineral.*, *86*(4), 385–391.

Yoshida, M., and A. Kageyama (2004), Application of the Yin-Yang grid to a thermal convection of a Boussinesq fluid with infinite Prandtl number in a three-dimensional spherical shell, *Geophys. Res. Lett.*, *31*(12), L12609, doi:10.1029/2004GL019970.

Yoshida, M., S. Honda, M. Kido, and Y. Iwase (2001), Numerical simulation for the prediction of the plate motions: Effects of lateral viscosity variations in the lithosphere, *Earth Planets Space*, *53*, 709–721.

Zhang, S., and U. Christensen (1993), Some effects of lateral viscosity variations on geoid and surface velocities induced by density anomalies in the mantle, *Geophys. J. Int.*, *114*(3), 531–547, doi:10.1111/j.1365-246X.1993.tb06985.x.

Zhong, S., and G. F. Davies (1999), Effects of plate and slab viscosities on the geoid, *Earth Planet. Sci. Lett.*, *170*(4), 487–496.

Zhong, S., M. T. Zuber, L. Moresi, and M. Gurnis (2000), Role of temperature-dependent viscosity and surface plates in spherical shell models of mantle convection, *J. Geophys. Res.*, *105*(B5), 11,063–11,082, doi:10.1029/2000JB900003.

Zhong, S., A. McNamara, E. Tan, L. Moresi, and M. Gurnis (2008), A benchmark study on mantle convection in a 3-D spherical shell using CitcomS, *Geochem. Geophys. Geosyst.*, *9*, Q10017, doi:10.1029/2008GC002048.